

# Direct Synthesis of Large-Area 2D Mo<sub>2</sub>C on In Situ Grown Graphene

Dechao Geng, Xiaoxu Zhao, Zhongxin Chen, Weiwei Sun, Wei Fu, Jianyi Chen, Wei Liu, Wu Zhou, and Kian Ping Loh\*

As a new member of the MXene group, 2D Mo<sub>2</sub>C has attracted considerable interest due to its potential application as electrodes for energy storage and catalysis. The large-area synthesis of Mo<sub>2</sub>C film is needed for such applications. Here, the one-step direct synthesis of 2D Mo<sub>2</sub>C-on-graphene film by molten copper-catalyzed chemical vapor deposition (CVD) is reported. High-quality and uniform Mo<sub>2</sub>C film in the centimeter range can be grown on graphene using a Mo–Cu alloy catalyst. Within the vertical heterostructure, graphene acts as a diffusion barrier to the phase-segregated Mo and allows nanometer-thin Mo<sub>2</sub>C to be grown. Graphene-templated growth of Mo<sub>2</sub>C produces well-faceted, large-sized single crystals with low defect density, as confirmed by scanning transmission electron microscopy (STEM) measurements. Due to its more efficient graphene-mediated charge-transfer kinetics, the as-grown Mo<sub>2</sub>C-on-graphene heterostructure shows a much lower onset voltage for hydrogen evolution reactions as compared to Mo<sub>2</sub>C-only electrodes.

2D transition-metal carbides belong to a family of chemical compounds called MXenes<sup>[1–5]</sup> and have attracted considerable interest in recent time as a new class of highly robust 2D materials with potential applications in energy storage and catalysis. One new important member of the MXene group is nanometer-thin Mo<sub>2</sub>C in which 2D superconductivity has been recently reported.<sup>[6–8]</sup> Nonetheless, the exploitation of MXenes in electronic applications requires the development of efficient

processes for the synthesis of MXene thin films with controlled structure and morphology. For example, Mo<sub>2</sub>C is currently prepared either by the high-temperature carburization of molybdenum oxides<sup>[9]</sup> or by chemically etching layered ternary Mo-containing phases.<sup>[10,11]</sup> In the former, processing at high temperature is necessary and the products usually contain a mixture of phases. In the latter method, 2D Mo<sub>2</sub>CT<sub>x</sub> (functionalized Mo<sub>2</sub>C, where T<sub>x</sub> denotes surface functionalization) is obtained by selectively etching ternary MAX phases with concentrated hydrofluoric acid, which gives rise to F or OH terminations on the surface. Both these methods have the disadvantage in that the as-prepared Mo<sub>2</sub>C sheets have small crystal sizes and nonuniform thicknesses. On the other hand, the high electron density at the Fermi level implies that MXene can be exploited for catalysis, moreover, theoretical studies have predicted that ferromagnetic or antiferromagnetic Ti or Cr carbide phases can be prepared if the surface F or OH terminations can be eliminated. In this context, chemical vapor deposition (CVD) offers the possibility to grow these 2D MXene films free from F or OH terminations. In addition, it will be interesting to prepare 2D vertical heterostructures of MXenes and other 2D materials for the study of charge transfer or proximity effects.

Herein, we demonstrate the one-step direct synthesis of large-area and uniform Mo<sub>2</sub>C crystals on in situ grown graphene substrates by ambient pressure CVD. The most important advantage of this method is that it circumvents the need for transfer processes, which are usually required for vertically stacked 2D heterostructures. We have shown that uniform large-area centimeter-scale Mo<sub>2</sub>C films can be grown on graphene. The Mo<sub>2</sub>C-on-graphene heterostructure shows enhanced catalytic activity in hydrogen evolution reaction (HER) compared to Mo<sub>2</sub>C-only catalyst due to efficient interfacial charge-transfer kinetics.

An ambient pressure CVD system is used for the preparation of the Mo<sub>2</sub>C–graphene hybrid or Mo<sub>2</sub>C-only sample. Liquid Cu<sup>[12]</sup> on the supporting Mo foil is used as the catalyst, methane (CH<sub>4</sub>) is the carbon precursor, and hydrogen (H<sub>2</sub>) is used as the reducing and carrier gas at the growth temperature of 1100 °C. The growth process is schematically shown in **Figure 1**. A Cu foil, which serves as the catalyst, is placed on the supporting Mo substrate and introduced into the quartz reactor. First, the

Dr. D. C. Geng, X. X. Zhao, Z. X. Chen, Dr. W. Fu, Dr. J. Y. Chen,  
Dr. W. Liu, Prof. K. P. Loh  
Department of Chemistry and Centre for Advanced 2D Materials  
National University of Singapore  
3 Science Drive 3, 117543, Singapore  
E-mail: chmlhkp@nus.edu.sg

Dr. W. W. Sun  
Department of Physics and Astronomy  
Vanderbilt University  
Nashville, TN 37235, USA

Dr. W. W. Sun, Prof. W. Zhou  
Materials Science and Technology Division  
Oak Ridge National Lab  
Oak Ridge, TN 37831, USA

Prof. W. Zhou  
School of Physical Sciences  
CAS Key Laboratory of Vacuum Physics  
University of Chinese Academy of Sciences  
Beijing 100049, China

DOI: 10.1002/adma.201700072

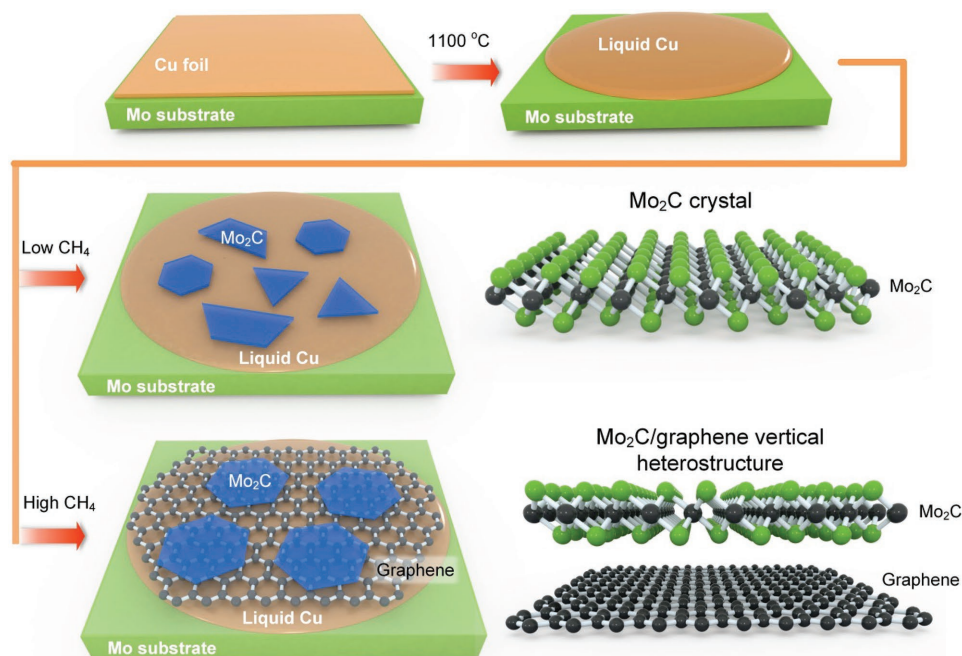


**Figure 1.** Schematic showing the growth of Mo<sub>2</sub>C crystals under low and high flow rates of CH<sub>4</sub>. Thick Mo<sub>2</sub>C crystals with different shapes are randomly distributed on the Cu surface at low CH<sub>4</sub> concentration, whereas at higher CH<sub>4</sub> concentration, the growth of predominantly hexagonal-shaped, thin Mo<sub>2</sub>C flakes on graphene is seen.

temperature is gradually increased to 1100 °C under a H<sub>2</sub> flow of 200 sccm and held at 1100 °C for 30 min. After this activation stage, crystal growth is initiated by introducing CH<sub>4</sub> into the chamber while maintaining the H<sub>2</sub> flow rate unchanged (see the Experimental Section). At temperatures >1086 °C, Cu melts, and due to its good wettability, covers the entire Mo substrate. The high reaction temperature results in the formation of a Cu–Mo alloy, through which surface segregation of Mo occurs. The segregated Mo further reacts with the carbon precursor to form Mo<sub>2</sub>C crystals. Different flow rates of CH<sub>4</sub> (0.3 and 3 sccm) have been performed to investigate the growth of Mo<sub>2</sub>C. Surprisingly, the as-grown Mo<sub>2</sub>C samples under the two growth conditions display big difference in both morphology and thickness (Figure 1). During the nucleation of Mo<sub>2</sub>C on the molten Cu surface, the flow rate of methane is adjusted to 0.3 sccm for 60 min. In this regime, the supply of carbon is rate-limiting and the surface segregated Mo scavenges the surface carbon to form Mo<sub>2</sub>C. This means that the growth rate of Mo<sub>2</sub>C is low and estimated to be 2 μm min<sup>-1</sup> (Figure S1, Supporting Information). If the flow rate of CH<sub>4</sub> is increased by one order of magnitude to reach the surface saturation limit, large monolayer graphene islands can be grown rapidly on liquid Cu (growth rate ≈21 μm min<sup>-1</sup>, based on first-nucleated graphene grains),<sup>[12]</sup> which drastically reduces the rate of diffusion of Mo toward the surface. In this growth regime, Mo atoms diffuse along the edges to basal plane of graphene and react with the impinging hydrocarbon molecules to form Mo<sub>2</sub>C crystals. Due to the slow diffusion of Mo atoms and since most of the surface sites are passivated by graphene, the growth rate of Mo<sub>2</sub>C is drastically reduced (by one order of magnitude as compared to the open Mo–Cu catalyst surface), thereby limiting

the final thickness of the Mo<sub>2</sub>C crystals to nanometers. Further, it is found out that the adsorption energy of CH<sub>4</sub> molecule on Mo<sub>2</sub>C (001) thin film is about 0.3 eV lower than that on graphene.<sup>[13,14]</sup> So the CH<sub>4</sub> molecules would prefer to adsorb on the formed Mo<sub>2</sub>C surface in both cases instead of to the Cu/Mo or graphene surface, leading to an expansion of Mo<sub>2</sub>C vertically but not laterally.

The morphology of Mo<sub>2</sub>C crystals is strongly influenced by the CH<sub>4</sub> flow rate. At low methane flux, the growth is inhomogeneous (Figure 2a) and there is a wide distribution of triangular, rectangular, pentagonal, and even fractal shapes (Figure S2a, Supporting Information). The thickness of the as-grown crystals is in the range of several hundred nanometers as measured by atomic force microscopy (AFM). Figure 2b shows the AFM image of a typical hexagonal crystal with a thickness of 237 nm. Figure 2c shows the statistical distribution of the flake thickness, which is in the 170–250 nm range.

At higher methane flux, the growth kinetics is influenced by the presence of graphene. First, it can be seen that the as-grown Mo<sub>2</sub>C crystals on graphene are extremely uniform both with respect to morphology and thickness (Figure 2d). Nearly 90% of the Mo<sub>2</sub>C crystals have hexagonal shape (Figure S2b, Supporting Information), compared to 40% without graphene. Second, the Mo<sub>2</sub>C flakes are of uniform thickness, i.e., ≈8 nm (Figure 2e,f), suggesting that graphene is highly effective in suppressing high growth rate channels by inhibiting the reaction of surface segregated Mo atoms with the hydrocarbon precursor (Figure S3, Supporting Information). Serving as a blocking layer, graphene can drastically reduce the thickness of as-grown Mo<sub>2</sub>C onto it, as schematically shown in Figure 2g.

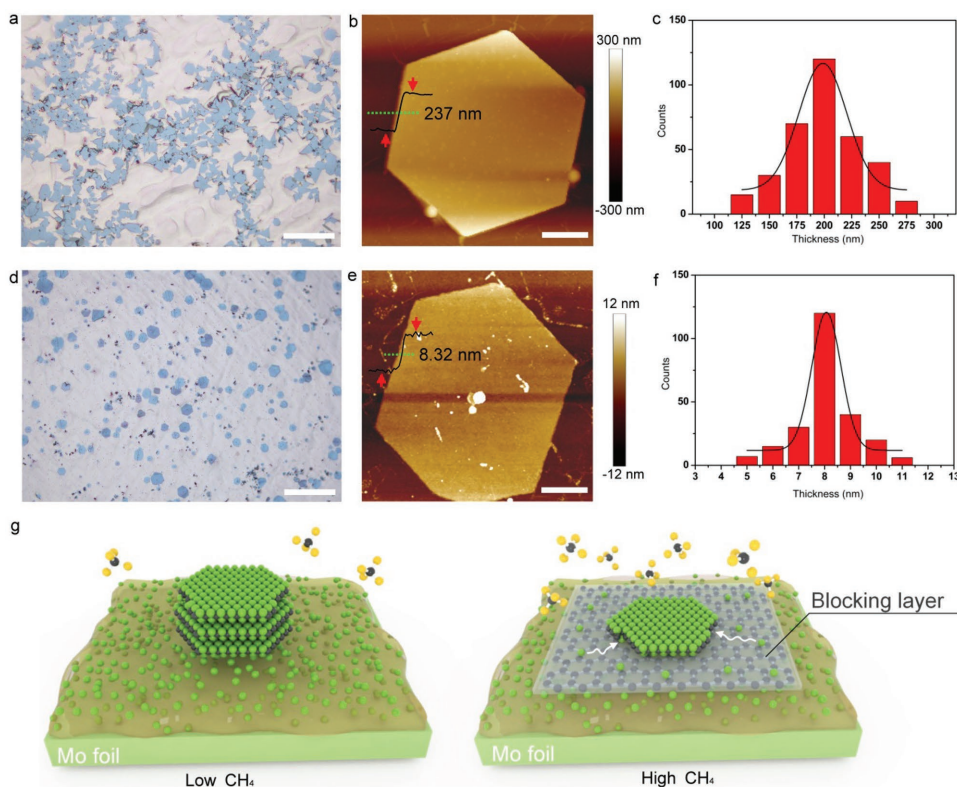


**Figure 2.** Thickness and shape control of  $\text{Mo}_2\text{C}$  by regulating the flow rate of  $\text{CH}_4$ . a,d) Optical images of  $\text{Mo}_2\text{C}$  crystals on Cu surface and graphene under low (a) and high (d) flow rate of  $\text{CH}_4$ . The images show differently shaped  $\text{Mo}_2\text{C}$  crystals grown on Cu, while the  $\text{Mo}_2\text{C}$  crystals grown on graphene are predominantly hexagonal shaped. b,e) AFM images of hexagonal  $\text{Mo}_2\text{C}$  crystals on Cu surface (b) and on graphene (e). c,f) Thickness distributions of the  $\text{Mo}_2\text{C}$  crystal grown on Cu (c) or graphene (f).  $\text{Mo}_2\text{C}$ -on-graphene crystals show a narrow thickness distribution of  $\approx 8 \pm 2$  nm. g) The schematic showing the growth mechanism of  $\text{Mo}_2\text{C}$  at low and high  $\text{CH}_4$ , respectively. Note that at high  $\text{CH}_4$  condition, graphene serves as a blocking layer, cutting off the vertical supply of Mo, resulting in the drastically decreased thickness of  $\text{Mo}_2\text{C}$  grown on it. The scale bars in (a) and (d) are 100  $\mu\text{m}$ , and in (b) and (e) are 1  $\mu\text{m}$ .

After CVD growth, the as-grown  $\text{Mo}_2\text{C}$ /graphene hybrid structures were transferred onto 300 nm  $\text{SiO}_2/\text{Si}$  substrates using the chemical etching method (see the Experimental Section). The shape of the  $\text{Mo}_2\text{C}$  crystals is maintained after transfer, indicating that the transfer process is efficient (Figure 3a,d insets). On  $\text{SiO}_2$ , the  $\text{Mo}_2\text{C}$  crystal can be easily distinguished from graphene due to its optical contrast (Figure S4, Supporting Information). They show different colors on  $\text{SiO}_2/\text{Si}$  substrates under an optical microscope (Figure S5a,b, Supporting Information), which allows rapid thickness identification. AFM imaging further confirms that the color contrast can be served as an indicator of thickness (Figure S5c,d, Supporting Information). X-ray photoelectron spectroscopy (XPS) measurements confirmed that the transferred crystals are composed of stoichiometric  $\text{Mo}_2\text{C}$  (Figure S6, Supporting Information).

Raman mapping was carried out to identify the phases and to verify the presence of graphene and  $\text{Mo}_2\text{C}$  in the vertical heterostructures. Figure 3 shows the typical Raman spectra of the transferred  $\text{Mo}_2\text{C}$  crystal on  $\text{SiO}_2/\text{Si}$  substrate. The optical images of crystals of  $\text{Mo}_2\text{C}$  and  $\text{Mo}_2\text{C}$ -on-graphene are presented in insets of Figure 3a,d, respectively. In the case of  $\text{Mo}_2\text{C}$  grown at a lower  $\text{CH}_4$  flow rate, Raman mapping allows us to distinguish  $\text{Mo}_2\text{C}$  (purple) from the  $\text{SiO}_2/\text{Si}$  substrate (green). Raman mapping in Figure 3b,c shows that the whole hexagonal

crystal is uniformly colored (false color) when mapped at the Raman peak position of  $650 \text{ cm}^{-1}$ , which can be assigned to the stretching modes of  $\text{Mo}_2\text{C}$ .<sup>[15]</sup> For the vertical heterostructures prepared under high methane flux, Raman signals due to both  $\text{Mo}_2\text{C}$  and graphene can be detected on the hexagonal-shaped crystal (Figure 3d). The G and 2D peaks of graphene can be detected at  $1590$  and  $2690 \text{ cm}^{-1}$  in the region shown by a blue dot outside the  $\text{Mo}_2\text{C}$  crystal (Figure 3d). This result is consistent with the conclusion that the growth of large area graphene passivates the catalyst surface. The Raman spectra from the red-dot area show signals due to both monolayer graphene and  $\text{Mo}_2\text{C}$ , demonstrating the successful integration of the vertical heterostructure (Figure 3e,f). Interestingly, we observed that the  $\text{Mo}_2\text{C}$  crystals are weakly bonded to graphene and occasionally fall off during transferring process (Figure S7, Supporting Information), leaving behind hexagonal traces. Raman spectroscopy confirmed the absence of  $\text{Mo}_2\text{C}$  in these areas (Figure S8, Supporting Information). The observation further confirms that the  $\text{Mo}_2\text{C}$  crystals are grown on the graphene film.

To grow large area  $\text{Mo}_2\text{C}$ , the growth conditions were optimized to facilitate a 2D growth, as illustrated in Figure 4. As schematically shown in Figure 4a, during the initial stage of the CVD process, graphene domains grow at a higher rate

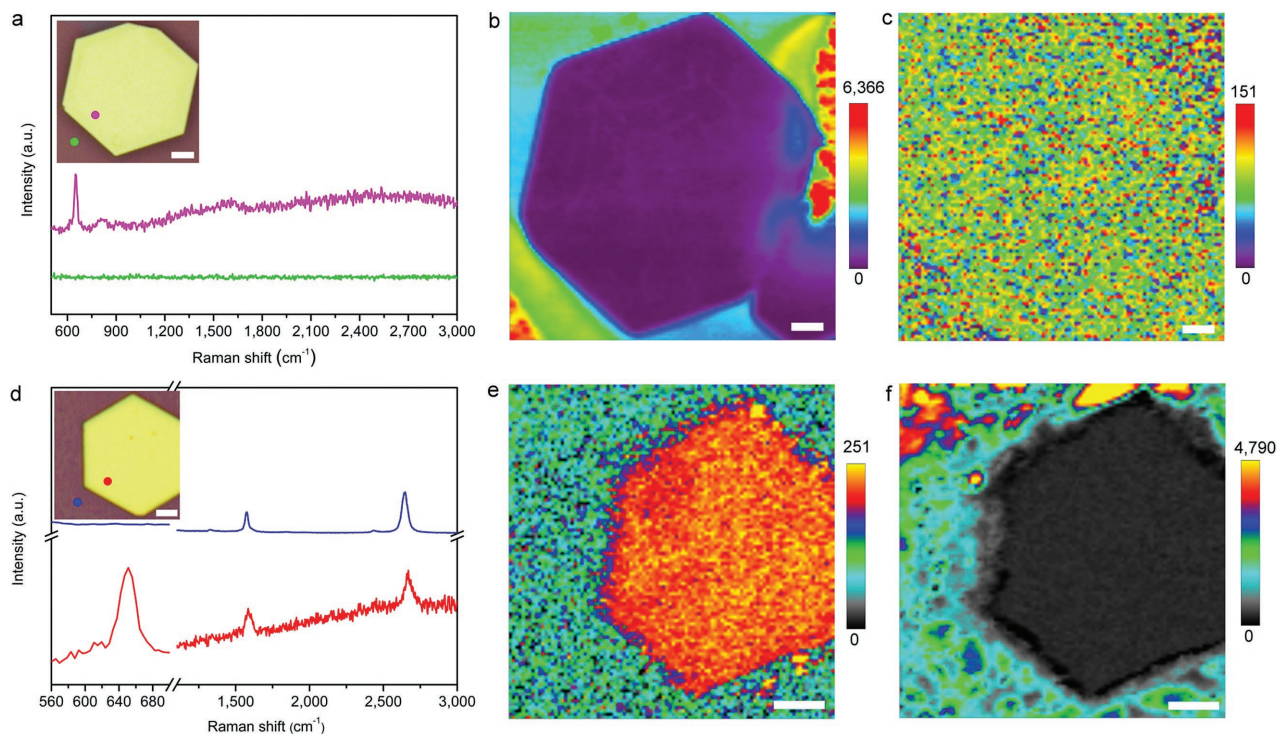


**Figure 3.** Raman mapping of as-grown  $\text{Mo}_2\text{C}$  grains. a) Raman spectrum recorded on areas marked with pink and green dots shown in the insets. The purple spectrum corresponds to the area marked by the purple dot on the crystal (inset) and shows a distinct signal due to  $\text{Mo}_2\text{C}$ , and the green area is composed of  $\text{SiO}_2/\text{Si}$ . b,c) Raman mapping of the  $\text{Mo}_2\text{C}$  flake at the peak positions  $650$  (b) and  $2690\text{ cm}^{-1}$  (c), indicating the presence of  $\text{Mo}_2\text{C}$  and the absence of graphene. d) Raman spectrum of the area denoted by a blue dot on the crystal (inset) shows signals from monolayer graphene, whereas regions marked with a red dot show Raman signatures of both  $\text{Mo}_2\text{C}$  and graphene. e,f) Raman mapped images of  $\text{Mo}_2\text{C}$ -on-graphene where the orange false color maps the  $\text{Mo}_2\text{C}$  signal at  $650\text{ cm}^{-1}$  (e) and the gray false color maps graphene signal at  $2690\text{ cm}^{-1}$  (f). All the scale bars are  $2\text{ }\mu\text{m}$ .

compared to  $\text{Mo}_2\text{C}$  on the liquid Cu surface and assemble to form a film. Subsequently,  $\text{Mo}_2\text{C}$  grains begin to nucleate on the in situ grown graphene substrate. With increasing time of reaction,  $\text{Mo}_2\text{C}$  grains nucleate, grow and finally coalesce into a continuous film. This suggests that a time dependent 2D growth mode is operative. The corresponding optical images recording the evolution of the crystal morphology with time and changing from isolated crystals into a fully coalesced film are displayed in Figure 4b–e. After a growth time of 10 min, as shown in Figure S9 (Supporting Information), the first-grown graphene domains have nearly coalesced to form a film, while  $\text{Mo}_2\text{C}$  just begins to nucleate at certain areas of graphene. Notably, it is found that the  $\text{Mo}_2\text{C}$  crystals are highly aggregated at the edged area of the substrate as shown in Figure S10 (Supporting Information). On the basis, the Mo atoms are likely to cross over the edged area of graphene and then diffuse onto the as-grown graphene. It is seen that the typical widths of the hexagonal  $\text{Mo}_2\text{C}$  grains after 30 min of growth reach  $50\text{ }\mu\text{m}$ , and grains with dimensions up to  $100\text{ }\mu\text{m}$  are obtained after 60 min growth time. All the grains are hexagonal-shaped (Figure 4c,d), and transmission electron microscopy (TEM) measurements confirmed that these are single crystals. Notably, no defects, disorders or impurities are observed even over a large area (Figure 4f–i and raw data in Figure S11, Supporting Information), indicating the very high quality and uniformity of our  $\text{Mo}_2\text{C}$  crystals. The above observations strongly suggest that

graphene can exercise a significant shape control in the growth of  $\text{Mo}_2\text{C}$  and promotes uniform and regular growth. The introduction of graphene can also offer a facile and effective way to realize large-scale  $\text{Mo}_2\text{C}$  crystals and uniform films.

To ascertain if graphene plays any role in influencing the surface crystallization of  $\text{Mo}_2\text{C}$  crystals, scanning transmission electron microscopy annular dark-field (STEM-ADF) imaging was performed both on  $\text{Mo}_2\text{C}$  crystals and on  $\text{Mo}_2\text{C}$ -on-graphene crystals, as shown in Figure 5. A typical STEM-ADF image of the edge region of  $\text{Mo}_2\text{C}$  crystals grown directly on molten Cu foil is depicted in Figure 5a, where a distinct dendritic structure is seen. The shape and thickness of the dendrites are irregular and nonuniform, pointing to inhomogeneous growth at the edge region. An irregular stripe-like second layer is formed on the surface and large thickness variations are seen, showing a very high Z-contrast difference.<sup>[16]</sup> It can therefore be concluded that both edges and bulk regions in  $\text{Mo}_2\text{C}$  crystals grown directly on the Mo–Cu catalyst are irregular and inhomogeneous.

The  $\text{Mo}_2\text{C}$  crystals which are grown on Mo–Cu catalyst present a translational stacking scheme as shown in Figure 5b. Such a translation defect is generally created by nanometer-wide strained channels. Geometric phase analysis (GPA) is further applied to analyze the level of strain associated with the grain boundaries.<sup>[17]</sup> A symmetric strain matrix series ( $\epsilon_{xx}$ ,  $\epsilon_{xy}$ ,  $\epsilon_{yy}$ , and rotation $_{xy}$ ) is used to map the strain fields and

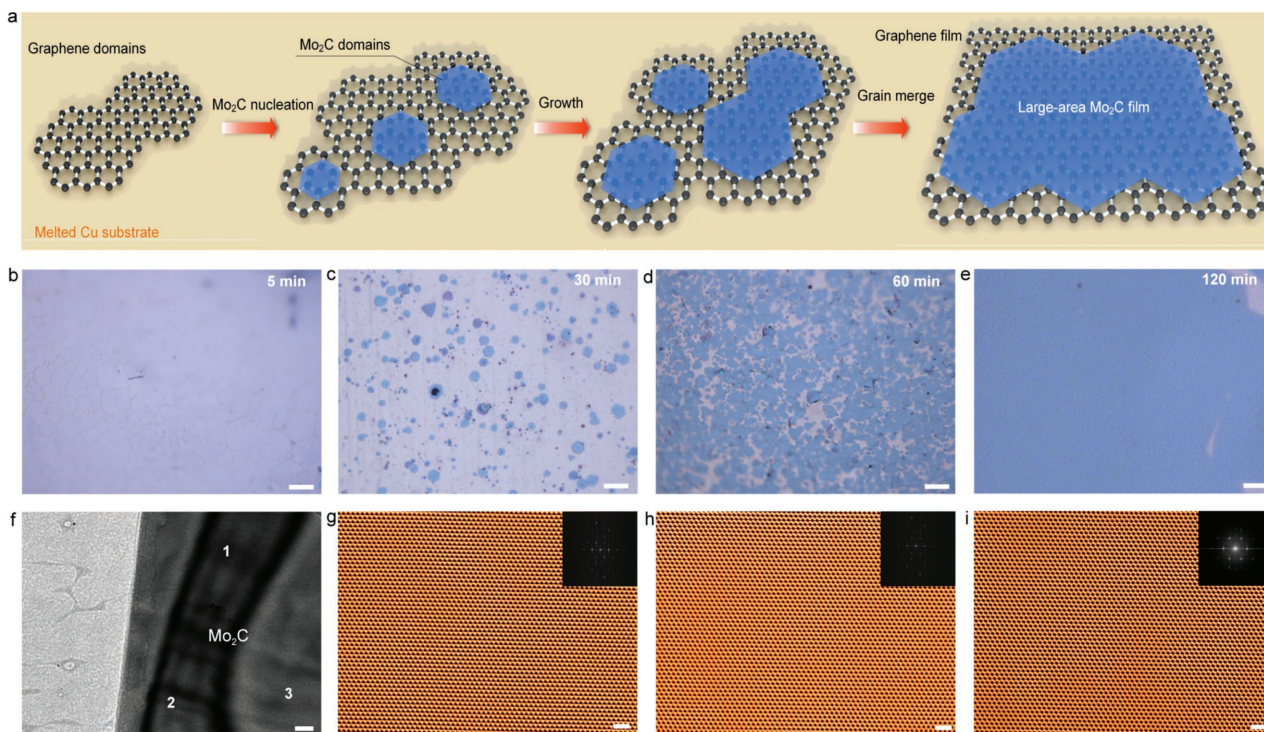


**Figure 4.** The growth of large-area  $\text{Mo}_2\text{C}$  crystals and film. a) Schematic showing the nucleation and coalescence of  $\text{Mo}_2\text{C}$  crystals grown on graphene. b–e) Typical optical images of  $\text{Mo}_2\text{C}$  grains on graphene for growth times of 5, 30, 60, and 120 min, respectively, with 3 sccm  $\text{CH}_4$  at  $1100^\circ\text{C}$ . It should be noted that all the grains are hexagonal shaped, suggesting that graphene may play the role of a template in controlling the shape of the crystals. f) TEM image of the as-grown  $\text{Mo}_2\text{C}$  film. g–i) Filtered atomic-level images of the three labeled areas in (f) all showing high-quality and uniformity over a large area. The scale bars in (b–e) are  $100\ \mu\text{m}$ , (f) is  $1\ \mu\text{m}$ , and (g–i) are  $1\ \text{nm}$ .

the results are given in the subpanel in Figure 5c. Apparently, maze-like strain fields are reflected in the entire symmetric strain matrix and dozens of point defects are seen decorating the whole area. Hence, it can be concluded that  $\text{Mo}_2\text{C}$  crystals which are grown directly on liquid Cu foil possess a high density of strain and also a high defect density. Moreover, as seen in Figure 5a, bright clusters are occasionally found distributed on the sample. Electron energy loss spectroscopy elemental mapping (Figure S12, Supporting Information) revealed that these are Mo clusters. It is believed that such Mo clusters could be formed due to inhomogeneous carbonization during growth. The step edges in Figure 5b are irregular and many Mo clusters frequently accumulated near the step edges (Figure S13, Supporting Information).  $\text{Mo}_2\text{C}$  crystals also exhibit a nonuniform dendritic edge structure and possess an inhomogeneous inner bulk region with a high concentration of defects and strain.

By contrast, Figure 5d shows that  $\text{Mo}_2\text{C}$  edges for  $\text{Mo}_2\text{C}$ -on-graphene crystal are extremely sharp and uniform, and the inner region is highly homogeneous without any obvious structural defect. The atomic structure of the as-prepared  $\text{Mo}_2\text{C}$ /graphene crystals is studied using STEM-ADF. It is clear that in this case, the  $\text{Mo}_2\text{C}$  crystals are homogeneously stacked without translational defects. Based on these observations, we infer that the presence of graphene modifies the growth mechanism from a precipitation-limited to a diffusion-limited process. In the case of  $\text{Mo}_2\text{C}$  growth on the

Mo–Cu catalyst, the growth rate depends on the rate of Mo precipitation from the molten alloy catalyst. In the presence of graphene, the surface of the catalyst is passivated and this inhibits the reaction of the surface-precipitated Mo atoms with gaseous hydrocarbon. Hence, the only way for growth to proceed is by the diffusion of Mo atoms to the edge and surface of graphene, whereupon it can react with the hydrocarbon precursor, which means that the surface crystallization of  $\text{Mo}_2\text{C}$  on graphene occurs at a much slower rate and can reach thermodynamic equilibrium, allowing well-faceted hexagonal shaped crystals to develop.

Strain analysis was performed on  $\text{Mo}_2\text{C}$ /graphene using GPA, similar to that applied for  $\text{Mo}_2\text{C}$  as shown in Figure 5c. The contrast between Figure 5c and Figure 5f is evident. No strain is detected in the  $\text{Mo}_2\text{C}$ /graphene heterostructure and it preserves an extremely high crystallinity. Step edges have also been imaged and these are atomically sharp (Figure S14, Supporting Information). STEM-ADF has also been conducted on the bulk regions for  $\text{Mo}_2\text{C}$ /graphene and  $\text{Mo}_2\text{C}$  grown directly on Mo/Cu catalyst, where a lower degree of strain was found in the former (Figure S15, Supporting Information). Therefore, it can be concluded that in the presence of the graphene, the crystallinity, homogeneity, and uniformity of CVD grown  $\text{Mo}_2\text{C}$  crystals are greatly enhanced. This implies that uniform carbon diffusion takes place on the graphene substrate during CVD growth, which leads to the formation of high-quality  $\text{Mo}_2\text{C}$  crystals.

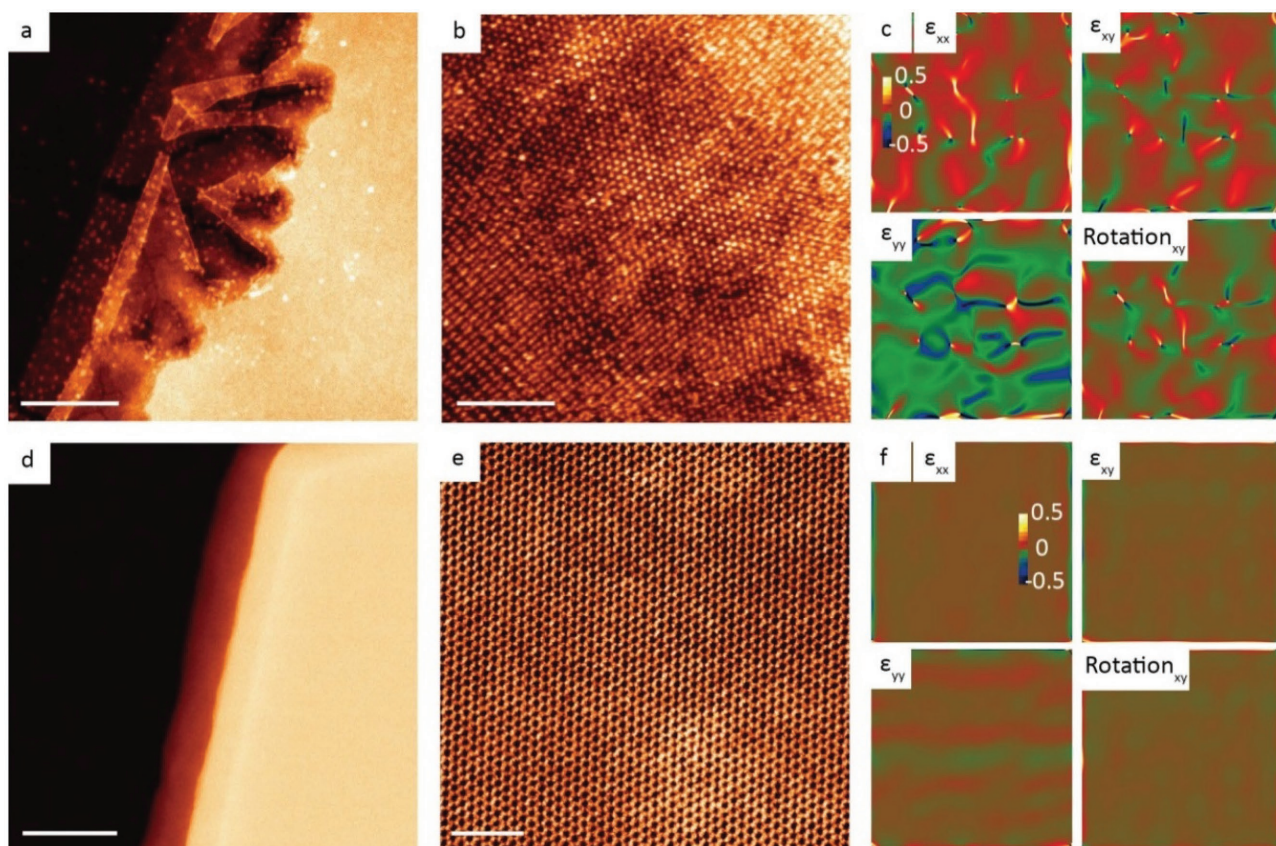


**Figure 5.** Comparison of the crystallinity of Mo<sub>2</sub>C and the vertical hetero-Mo<sub>2</sub>C/graphene structure. a) STEM-ADF image of a typical edge region in the Mo<sub>2</sub>C crystal and b) magnified image of a selected region in (a). c) Strain field mapping based on the image shown in (b). d) STEM-ADF image of a typical edge region in a vertical hetero-Mo<sub>2</sub>C/Gr crystal and e) its magnified image. f) Strain field mapping based on the image shown in (e). The scale bars in (a) and (d) are 100 nm and those in (b) and (e) are 2 nm.

Mo<sub>2</sub>C is commonly used as a catalyst in hydrogen evolution reactions (HER).<sup>[18,19]</sup> A three-electrode system was used to evaluate the comparative HER electrocatalytic performances of 1 cm × 1 cm Mo<sub>2</sub>C/graphene film, as well as 1 cm × 1 cm Mo<sub>2</sub>C films directly grown on Cu/Mo catalyst, using 0.5 M H<sub>2</sub>SO<sub>4</sub> electrolyte and a scan rate of 2 mV s<sup>-1</sup>. The films were transferred onto a GC (glassy carbon) electrode for the tests. As shown in **Figure 6a**, the Mo<sub>2</sub>C/graphene electrode has a low overpotential value of 236 mV versus reversible hydrogen electrode (RHE) for a current density of 10 mA cm<sup>-2</sup> with an onset potential of 87 mV, against 320 and 189 mV in the case of the Mo<sub>2</sub>C-only electrode. The overpotential value at 10 mA cm<sup>-2</sup> is an important reference because a solar-light-coupled HER apparatus usually operates at 10–20 mA cm<sup>-2</sup> under standard conditions (1 sun, AM 1.5). The Mo<sub>2</sub>C/graphene electrode has a Tafel slope of 73 mV dec<sup>-1</sup> as compared to 76 mV dec<sup>-1</sup> in the case of Mo<sub>2</sub>C (Figure 6b). The Tafel plots further indicate that hydrogen evolution on the Mo<sub>2</sub>C/graphene electrode probably follows a Volmer–Heyrovsky mechanism, where the electrochemical desorption of adsorbed H\* is the rate-limiting step.<sup>[20,21]</sup> To probe the durability of the Mo<sub>2</sub>C/graphene electrode, continuous CV was performed between -0.1 and 0.5 V at 100 mV s<sup>-1</sup> scan rate in 0.5 M H<sub>2</sub>SO<sub>4</sub> solution (Figure 6c). As can be observed, the polarization curve of the Mo<sub>2</sub>C/graphene electrode remains

unchanged even after 1000 cycles, pointing to the high stability of the electrode. By comparing the overpotential at 10 mA cm<sup>-2</sup>, it is clearly seen that the Mo<sub>2</sub>C/graphene electrode shows a more superior HER performance (Figure 6d and Table S1 (Supporting Information)) as compared to transition metal dichalcogenide-based 2D materials.<sup>[22–26]</sup> Since Mo<sub>2</sub>C/graphene is highly crystalline and contains nearly no defect, disorder, or impurity, we can infer that defects are not responsible for the superior HER activity. Instead, the enhanced HER performance of the Mo<sub>2</sub>C/graphene should be attributed to the high crystallinity of the Mo<sub>2</sub>C film, as well as its excellent electronic coupling to graphene in the vertically integrated structure, which acts as a charge relay system in the HER reaction.

In summary, the one-step direct growth of large-area and uniform Mo<sub>2</sub>C crystals on in situ grown graphene has been demonstrated. Using molten Mo–Cu alloy catalyst in CVD allows for the simultaneous growth of two 2D materials and is an easy way to vertically integrate ultrathin Mo<sub>2</sub>C crystals on graphene. The passivation of the catalyst surface by graphene during CVD prevents the segregated Mo from reacting with gaseous hydrocarbon, thus changing the growth from a precipitation-limited to a diffusion-limited process, which allows to better control the thickness of the Mo<sub>2</sub>C crystals on the nanometer scale. Graphene-templated growth of Mo<sub>2</sub>C produces

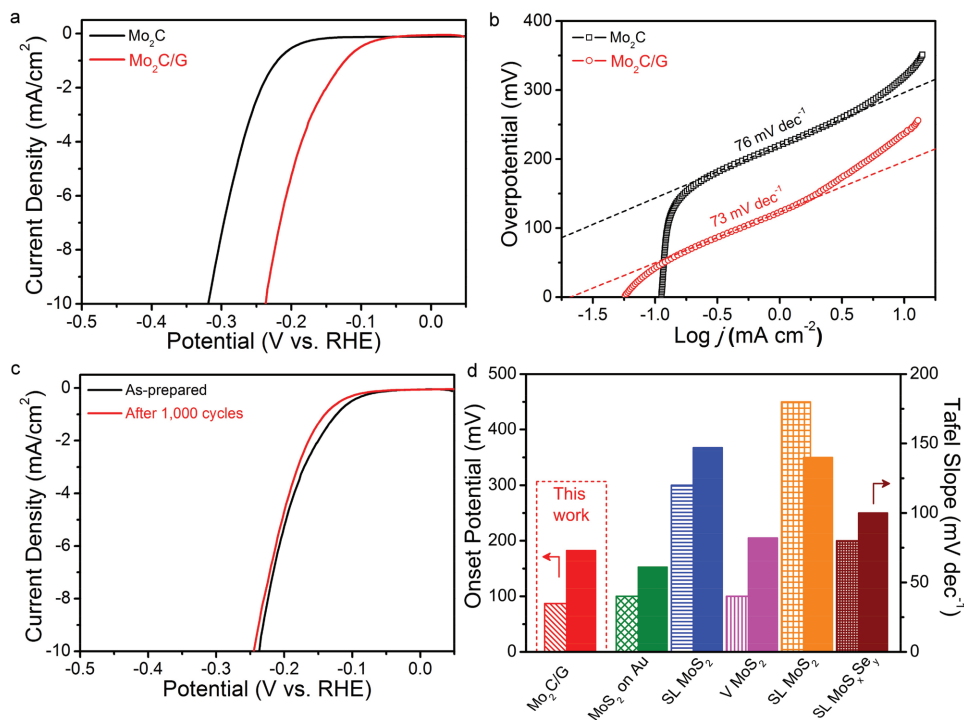


**Figure 6.** HER activity characterization. a,b) Polarization curves and Tafel plots of Mo<sub>2</sub>C and Mo<sub>2</sub>C/graphene. c) Polarization curves of Mo<sub>2</sub>C/graphene in the 1st cycle and after 1000 CV cycles. d) Comparison of the performance obtained in this work with other Mo-based catalysts. The given current density is normalized to the coverage of catalyst on the GC electrode (40%). The Tafel slope and onset potential value are calculated from the normalized data.

well-faceted, large-sized single crystals with low defect density as confirmed by STEM measurements. Finally, compared to other 2D materials, Mo<sub>2</sub>C–graphene heterostructure shows a superior HER performance. The integration of MXenes on graphene using this novel CVD approach is an important step forward to prepare large area MXenes–graphene heterostructures, where the synergy between the two 2D materials can be exploited.

## Experimental Section

**CVD Growth of Mo<sub>2</sub>C/Graphene Heterostructures:** A Cu foil (Alfa Aesar, 99.8% purity, 50 μm thick) was cut into 10 × 10 mm<sup>2</sup> pieces and placed on top of a Mo foil (Alfa Aesar, 99.95% purity, 50 μm thick) of the same size. They were then placed in a quartz tube of outer diameter 25 mm, inner diameter 22 mm, and length 1220 mm to act as catalyst for growth of Mo<sub>2</sub>C crystals. Subsequently, the substrates were heated above 1100 °C in a horizontal tube furnace (Lindberg Blue M, TF55030C) under 200 sccm H<sub>2</sub>. 3 sccm CH<sub>4</sub> was then introduced into the chamber at ambient pressure to initiate the growth of heterostructure. Large-area vertical structures could be grown using a longer growth time of 2 h. After the reaction, the samples were quickly removed from the high-temperature zone under H<sub>2</sub>, to ensure rapid cooling of the samples to room temperature.

**Transfer of Mo<sub>2</sub>C and Mo<sub>2</sub>C/Graphene Heterostructures:** Poly(methyl methacrylate) (PMMA)-assisted chemical etching method was used. A thin layer of PMMA (weight-averaged molecular mass  $M_w = 600\,000$ , 4 wt% in ethyl lactate) was first spin-coated on the surface of Mo<sub>2</sub>C crystals at 6000 rpm for 3 min and cured at 170 °C for 5 min; the PMMA-coated samples were immersed into a 1 M (NH<sub>4</sub>)<sub>2</sub>S<sub>2</sub>O<sub>8</sub> aqueous solution for etching the underneath Mo and Cu substrates. Then the PMMA/Mo<sub>2</sub>C

layer was detached from the substrate after several minutes. After cleaning with pure water, the floating PMMA/Mo<sub>2</sub>C layer was stamped at the target substrate, such as SiO<sub>2</sub>/Si and TEM grids. Finally, the PMMA was removed by warm acetone, obtaining clean ultrathin Mo<sub>2</sub>C crystals.

**Characterization:** Optical images were obtained using an Olympus BX51 microscope. AFM images were obtained using a Bruker Dimension FastScan atomic force microscope in the tapping mode. XPS analysis was carried out on an Omicron EAC2000-125 analyzer. Base pressure during analysis was 10<sup>−9</sup> Torr. An Al K<sub>α</sub> monochromatized radiation ( $h\nu = 1486.6$  eV) was employed as the X-ray source. Raman spectra were recorded at room temperature using a WITec Raman microscope with laser excitation at 532 nm. Bright-field TEM images of Mo<sub>2</sub>C flakes were conducted on Philips CM30 TEM at 300 kV. High resolution STEM-ADF imaging was carried on an aberration-corrected Nion UltraSTEM-100, equipped with a cold field emission gun, operating at 100 kV for Mo<sub>2</sub>C samples.

**Hydrogen Evolution Reaction Measurements:** HER measurements were performed at room temperature in a three-electrode cell using an Ag/AgCl electrode and a Pt foil as the reference and the counter electrode. Mo<sub>2</sub>C/graphene foils were transferred onto a glassy carbon plate as the working electrode. Linear sweep voltammetry with a scan rate of 2 mV s<sup>−1</sup> was recorded in 0.5 M H<sub>2</sub>SO<sub>4</sub> electrolyte on an Autolab 302N electrochemical workstation. Cycling stability was evaluated by a continuous 1000 cycling from −0.1 to 0.5 V at a scan rate of 100 mV s<sup>−1</sup>. The HER data are all normalized according to the coverage of catalyst on the GC electrode (40%). All potentials were calibrated with respect to RHE.

## Supporting Information

Supporting Information is available from the Wiley Online Library or from the author.

## Acknowledgements

K.P.L. acknowledges the NRF investigator award “Graphene oxide—A new class of catalytic, ionic and molecular sieving materials” R-143-000-610-281.

## Conflict of Interest

The authors declare no conflict of interest.

## Keywords

2D Mo<sub>2</sub>C, graphene, molten Cu–Mo alloys, vertical heterostructures

Received: January 5, 2017

Revised: May 10, 2017

Published online:

- [1] M. R. Lukatskaya, O. Mashtalir, C. E. Ren, Y. Dall'Agnese, P. Rozier, P. L. Taberna, M. Naguib, P. Simon, M. W. Barsoum, Y. Gogotsi, *Science* **2013**, *341*, 1502.
- [2] M. Ghidui, M. R. Lukatskaya, M. Q. Zhao, Y. Gogotsi, M. W. Barsoum, *Nature* **2014**, *516*, 78.
- [3] M. Naguib, V. N. Mochalin, M. W. Barsoum, Y. Gogotsi, *Adv. Mater.* **2014**, *26*, 992.
- [4] M. Naguib, O. Mashtalir, J. Carle, V. Presser, J. Lu, L. Hultman, Y. Gogotsi, M. W. Barsoum, *ACS Nano* **2012**, *6*, 1322.
- [5] F. Shahzad, M. Alhabeab, C. B. Hatter, B. Anasori, S. M. Hong, C. M. Koo, Y. Gogotsi, *Science* **2016**, *353*, 1137.
- [6] C. Xu, L. B. Wang, Z. B. Liu, L. Chen, J. K. Guo, N. Kang, X. L. Ma, H. M. Cheng, W. C. Ren, *Nat. Mater.* **2015**, *14*, 1135.
- [7] L. B. Wang, C. Xu, Z. B. Liu, L. Chen, X. L. Ma, H. M. Cheng, W. C. Ren, N. Kang, *ACS Nano* **2016**, *10*, 4504.
- [8] D. C. Geng, X. X. Zhao, L. J. Li, P. Song, B. B. Tian, W. Liu, J. Y. Chen, D. Shi, M. Lin, W. Zhou, K. P. Loh, *2D Mater.* **2016**, *4*, 011012.
- [9] M. K. Kolel-Veetil, S. B. Qadri, M. Osofsky, T. M. Keller, *Chem. Mater.* **2005**, *17*, 6101.
- [10] J. Halim, S. Kota, M. R. Lukatskaya, M. Naguib, M. Q. Zhao, E. J. Moon, J. Pitock, J. Nanda, S. J. May, Y. Gogotsi, M. W. Barsoum, *Adv. Funct. Mater.* **2016**, *26*, 3118.
- [11] M. Naguib, R. R. Unocic, B. L. Armstrong, J. Nand, *Dalton Trans.* **2015**, *44*, 9353.
- [12] D. C. Geng, B. Wu, Y. L. Guo, L. P. Huang, Y. Z. Xue, J. Y. Chen, G. Yu, L. Jiang, W. P. Hu, Y. Q. Liu, *Proc. Natl. Acad. Sci. USA* **2012**, *109*, 7992.
- [13] Y. Shi, Y. Yang, Y. Li, H. Jiao, *Appl. Catal., A* **2016**, *524*, 223.
- [14] J. Schrier, *ACS Appl. Mater. Interfaces* **2011**, *3*, 4451.
- [15] T. C. Xiao, A. P. E. York, H. Al-Megren, C. V. Williams, H. T. Wang, M. L. H. Green, *J. Catal.* **2001**, *202*, 100.
- [16] O. L. Krivanek, M. F. Chisholm, V. Nicolosi, T. J. Pennycook, G. J. Corbin, N. Dellby, M. F. Murfitt, C. S. Own, Z. S. Szilagyi, M. P. Oxley, S. T. Pantelides, S. J. Pennycook, *Nature* **2010**, *464*, 571.
- [17] M. J. Hytch, E. Snoeck, R. Kilaas, *Ultramicroscopy* **1998**, *74*, 131.
- [18] H. Vrubel, X. Hu, *Angew. Chem., Int. Ed.* **2012**, *51*, 12703.
- [19] J. S. Li, Y. Wang, C. H. Liu, S. L. Li, Y. G. Wang, L. Z. Dong, Z. H. Dai, Y. F. Li, Y. Q. Lan, *Nat. Commun.* **2016**, *7*, e11204.
- [20] Z. X. Chen, K. Leng, X. X. Zhao, S. Malkhandi, W. Tang, B. B. Tian, L. Dong, L. R. Zheng, M. Lin, B. S. Yeo, K. P. Loh, *Nat. Commun.* **2017**, *8*, e14548.
- [21] Y. Zheng, Y. Jiao, M. Jaroniec, S. Z. Qiao, *Angew. Chem., Int. Ed.* **2015**, *54*, 52.
- [22] J. P. Shi, D. L. Ma, G. F. Han, Y. Zhang, Q. Q. Ji, T. Gao, J. Y. Sun, X. J. Song, C. Li, Y. S. Zhang, X. Y. Lang, Y. F. Zhang, Z. F. Liu, *ACS Nano* **2014**, *8*, 10196.
- [23] G. L. Ye, Y. J. Gong, J. H. Lin, B. Li, Y. M. He, S. T. Pantelides, W. Zhou, R. Vajtai, P. M. Ajayan, *Nano Lett.* **2016**, *16*, 1097.
- [24] H. Li, C. Tsai, A. L. Koh, L. L. Cai, A. W. Contryman, A. H. Fragapane, J. H. Zhao, H. S. Han, H. C. Manoharan, F. A. Pedersen, J. K. Nørskov, X. L. Zheng, *Nat. Mater.* **2016**, *15*, 48.
- [25] Y. F. Yu, S. Y. Huang, Y. P. Li, S. N. Steinmann, W. T. Yang, L. Y. Cao, *Nano Lett.* **2014**, *14*, 553.
- [26] L. Yang, Q. Fu, W. H. Wang, J. Huang, J. L. Huang, J. Y. Zhang, B. Xiang, *Nanoscale* **2015**, *7*, 10490.